

## Chapter 2

# Experimental Investigation on Strength Failure and Crack Evolution Behavior of Brittle Sandstone Containing a Single Fissure

In this chapter, in order to better understand the strength and fracture coalescence phenomena in brittle rock material, uniaxial compression experiments were conducted for brittle sandstone specimens containing a single fissure by a rock mechanics servo-controlled testing system. Moreover, this experiment relied on photographic monitoring and AE technique to obtain the real-time crack coalescence process in the process of the whole deformation failure, which was not performed for brittle sandstone in previous studies.

The emphasis of this chapter is focused on investigation of the influence of the geometry of single fissures (fissure length and fissure angle) on the strength and deformation failure behavior of brittle sandstone material, to analyze real-time crack coalescence process in real sandstone material under uniaxial compression on the basis of photographic monitoring and AE technique, and to study the effect of crack coalescence on the strength and deformation failure behavior of brittle sandstone specimens (Yang and Jing 2011).

## 2.1 Experimental Studies

### 2.1.1 Sandstone Material

To investigate the strength failure and crack coalescence behavior of rock containing a single fissure under uniaxial compression, sandstone material located in Linyi City, Shandong province of China was chosen for the experimental object in this chapter. The sandstone has a crystalline and blocky structure, which is a fine-grained heterogeneous material with average unit weight of about 2620 kg/m<sup>3</sup>. Moreover, the tested sandstone is porous. Based on the results of X-ray diffraction (XRD) (Fig. 2.1), the minerals in sandstone specimens are mainly feldspar, quartz, kaolinite, and chlorite; the detail composition of these rocks are given in Fig. 2.2.

**Fig. 2.1** XRD analysis of sandstone material in this chapter (with kind permission of Springer Publisher)

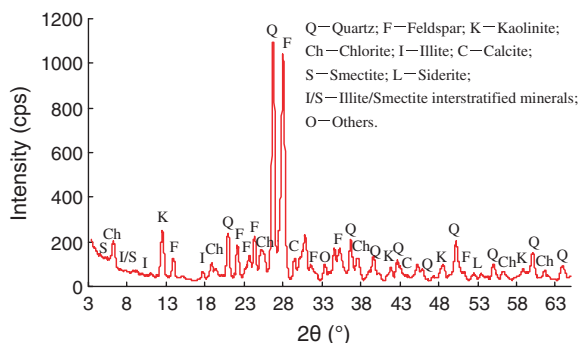
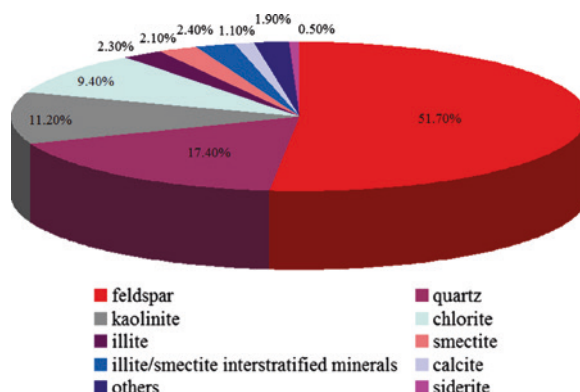


**Fig. 2.2** Composition (wt%) of sandstone. The mineralogical composition is derived from X-ray diffraction (XRD) (with kind permission of Springer Publisher)



### 2.1.2 Preparation for Specimen with Single Fissure

In this chapter, sandstone specimens containing a single fissure were prepared to carry out uniaxial compression tests. The specimens were cut from the same rectangular block. When cutting, the sandstone specimens were machined along the same direction in order to avoid the effect of anisotropy on the experimental results of sandstone. In order to obtain the exact results as well as the best comparison, all the tests were performed in natural and dry conditions.

Following the method suggested by the ISRM (Fairhurst and Hudson 1999), the height-to-width ratio of tested specimen should be in the range of 2.0–3.0 in order to minimize the effect of the end friction effects on the testing results. Therefore, the size of all tested sandstone specimens is rectangular with 120 mm in height, 60 mm in width, and 30 mm in thickness. As a result, all tested specimens with height-to-width ratio of 2.0 ensure a uniform stress state within the central part of the specimens.

The geometry of fissured sandstone is described in Fig. 2.3. Notice in this book, the term “fissure” is used to describe an artificially created flaw or crack; however, the term “crack” is adopted to describe the new fracture or failure in the process of loading. The geometry of single fissure is defined by two geometrical

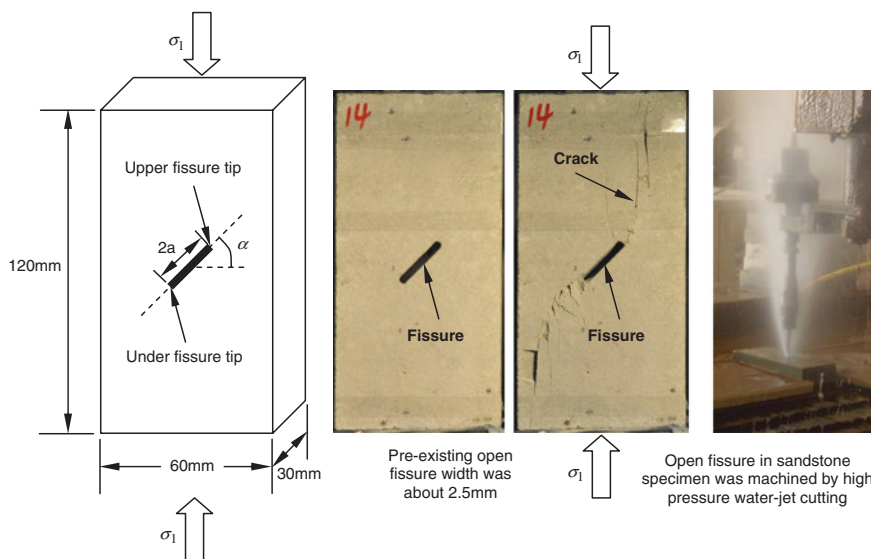


**Fig. 2.3** Geometry of single fissure in the sandstone specimens, in which  $\alpha$  is fissure angle,  $2a$  is fissure length. In this chapter, open fissure in sandstone specimen was machined by high pressure water-jet cutting (with kind permission of Springer Publisher)

parameters—fissure length  $2a$  and fissure angle (the angle of fissure with the direction of the horizontal direction)  $\alpha$  as shown in Fig. 2.3.

Although for rock-like materials, it is easier to make fissures by inserting steel or copper slices during the molding process, it is more difficult to cut fissures in the thick specimens of real rock (Li et al. 2005). High pressure water-jet cutting machine was used to cut open single fissures in the intact sandstone specimens. Machined open fissure width was about 2.5 mm. In order to investigate the effect of pre-existing single fissure geometry on the strength, deformation, and failure behavior of sandstone under uniaxial compression, different geometries of single fissure by varying one of the two parameters ( $2a$  and  $\alpha$ ) while keeping another constant were chosen in this chapter. Detailed description of sandstone specimens with different single fissure geometries is listed in Table 2.1.

### 2.1.3 Experimental Equipment and Procedure

Uniaxial compression experiments for intact and fissured sandstone specimens were carried out on a rock mechanics servo-controlled testing system (MTS815.02) with the maximum loading capacity of 2700 kN and the maximum displacement capacity of 25 mm, as shown in Fig. 2.4. This servo-controlled system can test specimens in load or displacement control while the data are recorded and analyzed in real-time. The axial stress was imposed on the surface

**Table 2.1** Pre-existing single fissure geometries of sandstone specimens under uniaxial compression

Specimen	W (mm)	H (mm)	T (mm)	M (g)	$\rho$ (kg/m <sup>3</sup> )	$\alpha^\circ$	2a (mm)	Note
GS-03 <sup>#</sup>	60.4	120.3	30.0	572.41	2625.9	N/A	0	Intact specimen
GS-04 <sup>#</sup>	60.1	120.4	29.8	559.54	2599.4	45	5	Fissure length
GS-07 <sup>#</sup>	60.2	120.8	29.0	551.09	2622.1	45	10	
GS-10 <sup>#</sup>	60.3	120.0	29.3	549.53	2605.4	45	15	
GS-14 <sup>#</sup>	60.3	120.5	30.1	567.32	2611.9	45	20	
GS-17 <sup>#</sup>	60.1	120.3	29.4	555.72	2637.2	45	25	
GS-19 <sup>#</sup>	60.5	120.0	29.9	571.30	2645.5	15	15	Fissure angle
GS-11 <sup>#</sup>	60.4	120.0	28.3	538.22	2637.6	45	15	
GS-25 <sup>#</sup>	60.5	120.2	29.9	561.64	2596.4	60	15	
GS-28 <sup>#</sup>	60.3	120.2	29.3	552.48	2615.0	75	15	

Note W Width; H Height; T Thickness; M Mass



**Fig. 2.4** MTS815.02 rock mechanics servo-controlled testing system and AE21C-06 acoustic emission system, in which the camera and lamp were used to record clearly the crack coalescence process of sandstone (with kind permission of Springer Publisher)

of rock specimen until failure took place. All the tests were conducted under displacement-controlled conditions with a strain rate of  $(1.3\text{--}2.0) \times 10^{-5}$ .

In this chapter, we measured axial force with loading capacity of 600 kN and axial deformation with displacement capacity of 5 mm. During the entire uniaxial compression experiments, loads and deformations of the tested sandstone specimens were recorded simultaneously. Moreover, two rigid steel blocks (63 mm wide, 32 mm thick, and 15 mm high) were placed between the loading frame and rock specimen. At the same time, two antifriction gaskets were placed between two rigid steel blocks and the end face of rock specimen, which decreased distinctly the effect of the end friction effects on the testing results of sandstone specimens of height-to-width ratio  $\sim 2.0$ .

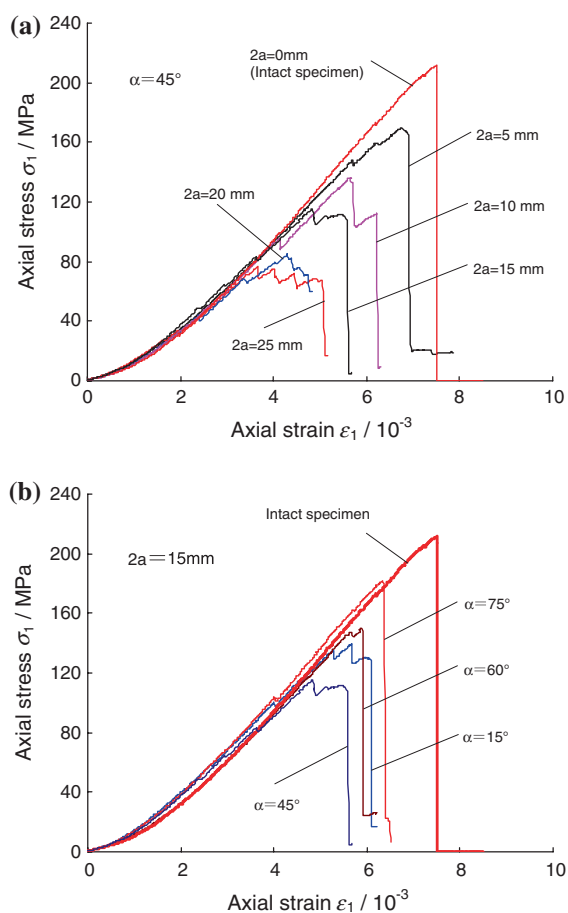
During the uniaxial compression test, in order to investigate the crack coalescence mechanism in the sandstone specimens containing single fissure, the AE technique was adopted. The AE counts and AE energy rate were recorded by AE21C-06 Acoustic Emission System (Fig. 2.4). The frequency of AE system

ranges from 5 kHz to 1 MHz and the recording event rate is 0.1 s. At the same time, the camera was used to trigger manually to capture images when the coalescence cracks developed or specimen failure occurred. When measuring AE signals, it is a pity that only one AE sensor was stuck on the sandstone specimens (Fig. 2.4) using Vaseline as a coupling agent and fixed slightly by cellulose tape, which is approximately similar to that of Li et al. (2005). Notice the AE sensor is near the pre-existing fissure in the specimen.

## 2.2 Strength and Deformation Behavior

Axial stress–axial strain curves for sandstone specimens containing single fissure under uniaxial compression are shown in Fig. 2.5, in which the axial stress–axial strain curve of intact sandstone specimen is also plotted. From Fig. 2.5, it is clear

**Fig. 2.5** Axial stress–axial strain curves of sandstone specimens containing a single fissure under uniaxial compression, in which (a) and (b), respectively, show the effect of fissure length and fissure angle on axial stress–axial strain curves (with kind permission of Springer Publisher)



that the fissure length and fissure angle have a key effect on the strength and deformation behavior of sandstone specimens under uniaxial compression, which will be analyzed in detail as follows.

### 2.2.1 Uniaxial Stress–Strain Curves of Sandstone

In accordance with the axial stress–axial strain curve shown in Fig. 2.5 and the failure mode plotted in Fig. 2.6, we can see that the sandstone in this chapter is a kind of brittle rock and takes on typically axial splitting failure, i.e., the axial stress drops abruptly to zero in 2 s after peak stress and a huge failure sonic can be heard during dropping. Notice the intact specimen was fractured into many small blocks under uniaxial compression. The axial stress–axial strain behavior of sandstone containing a single fissure can be approximately divided into four typical stages, i.e., fissure closure, elastic deformation, crack growth and propagation, and strain-softening.

In the stage of fissure closure, the uniaxial compression stress–strain curve of sandstone specimen containing different single fissure geometries shows the downward concave and the initial nonlinear deformation at low stress levels, which results from the closure of some primary pores and voids in the specimen with increasing compression stress. Moreover, the rigidity of the sandstone specimen at the initial stage of deformation (Fig. 2.5) has better consistency and is not dependent on fissure length and fissure angle, which results from better homogeneity of tested rock material. In the stage of elastic deformation, loading begins with increase in axial stress after the primary fissure closure in intact and flawed sandstone specimen, and elastic deformation dominates the stress–strain curve of

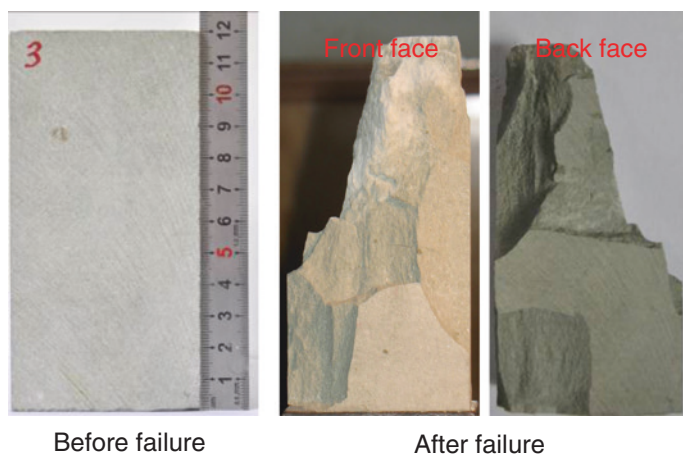


**Fig. 2.6** Typically axial splitting failure of intact sandstone specimen in this chapter (with kind permission of Springer Publisher)

specimen. The linear stress–strain behavior of intact and flawed sandstone specimen does not change although there are some irrecoverable processes such as the fissure closure or crack initiation at this stage. However, it needs to be noted that even at this stage of elastic deformation, some initiated cracks from the tips of fissure in flawed specimen have still been possible to propagate along the direction of axial stress, which is different from intact specimen.

However, at the stage of crack growth and propagation, the sandstone specimen continuously produces stress concentration near the tips of pre-existing single fissure, which result in some new cracks that initiate and propagate from the upper and under tips along the direction of axial stress. Therefore the stress–strain curve departs from the elastic behavior and shows distinct nonlinear deformation. In the stage of strain-softening, the macroscopic crack in intact and flawed sandstone specimen comes out rapidly and the post-peak behavior in the stress–strain curves shows a rapid drop. At this time, the specimen can only support lower axial stress, even though there is no axial stress.

It needs to be noted that the stress–strain curves of sandstone specimen containing single fissure show an abrupt change of slope before peak strength, which is coincident with the propagation of some cracks at the upper and under tips of pre-existing fissures. For the abrupt change in the stress–strain curve, we will make a detailed analysis and explanation in Sect. 2.4. Moreover, compared with intact specimen, specimens containing single fissure take on the localization deformation failure nearby peak strength, which is closely related to the fissure length and fissure angle. For specimens containing longer fissures (keeping  $\alpha = 45^\circ$ ) or larger fissure angles (keeping  $2a = 15$  mm), the localization deformation failure nearby peak strength is more distinct, as shown in Fig. 2.5.

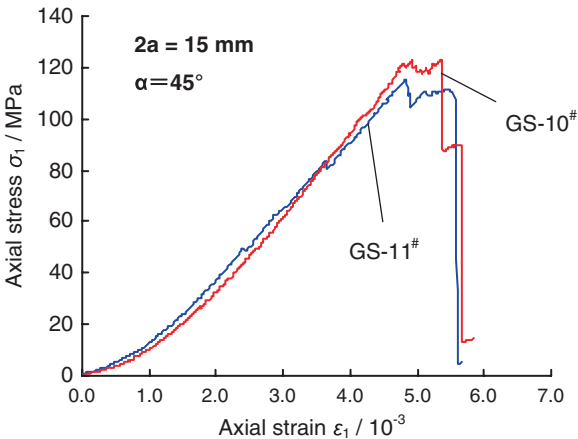
### ***2.2.2 Effect of Single Fissure Geometry on Mechanical Parameters of Sandstone***

In this section, the influence of single fissure geometry is investigated on the strength and deformation parameters of sandstone specimens under uniaxial compression, which are listed in detail in Table 2.2. Before analyzing the effect of single fissure geometry on strength and deformation parameters of sandstone, we first investigate the influence of heterogeneity of sandstone material on axial stress–axial strain curve of specimens containing a single fissure ( $2a = 15$  mm and  $\alpha = 45^\circ$ ) under uniaxial compression, which is presented in Fig. 2.7. From Fig. 2.7, the heterogeneity has nearly no effect on the strength and deformation parameters of two specimens containing the same single fissure, which have good consistency. Therefore, the dispersion of sandstone specimen containing a single fissure in this chapter is very small, and the strength and deformation parameters listed in Table 2.2 can be used to discuss approximately the effect of single fissure geometry on the mechanical parameters of sandstone under uniaxial compression. But due to limited tested specimens from the same block, we cannot repeat the

**Table 2.2** Mechanical parameters of sandstone specimens containing a single fissure under uniaxial compression

Specimen	$\alpha^\circ$	$2a$ (mm)	$\sigma_c$ (MPa)	$E_S$ (GPa)	$E_{50}$ (GPa)	$\varepsilon_{1c}(10^{-3})$	Note
GS-03#	N/A	0	212.08	35.95	24.37	7.500	Intact specimen
GS-04#	45	5	170.04	31.47	22.63	6.768	Fissure length
GS-07#	45	10	136.39	30.74	20.91	5.671	
GS-10#	45	15	122.80	28.61	20.54	5.358	
GS-14#	45	20	85.29	28.21	17.09	4.308	
GS-17#	45	25	77.25	28.56	16.81	3.674	
GS-19#	15	15	139.28	32.86	22.95	5.663	Fissure angle
GS-11#	45	15	115.17	28.11	21.13	4.827	
GS-25#	60	15	149.96	32.25	21.68	5.881	
GS-28#	75	15	181.71	33.97	24.93	6.348	

**Fig. 2.7** Effect of heterogeneity on axial stress–axial strain curve of sandstone specimens containing a single fissure ( $2a = 15$  mm and  $\alpha = 45^\circ$ ) under uniaxial compression (with kind permission of Springer Publisher)



test for other specimens of different fissure lengths and angles. Moreover, because sandstone is a kind of natural geological material; complete axial stress–axial strains of two specimens in Fig. 2.7 have some minor differences, which results from the effect of heterogeneity on the crack coalescence process of rock.

The definition for every mechanical parameter in Table 2.2 is described as follows.  $\sigma_c$  is defined as the uniaxial compressive strength and  $\varepsilon_{1c}$  is defined as peak axial strain value.  $E_S$  represents the elastic modulus; but  $E_{50}$  is defined as deformation modulus. More detailed descriptions of Young’s modulus can be found in (Yang and Jiang 2010). In accordance with Table 2.2, the effect of fissure length and fissure angle on the  $\sigma_c$ ,  $\varepsilon_{1c}$ ,  $E_S$ , and  $E_{50}$  of sandstone specimen containing a single fissure are analyzed and discussed in detail (Figs. 2.8 and 2.9). The uniaxial compressive strength, Young’s modulus and peak axial strain of sandstone specimens with pre-existing single fissure are all lower than that of intact sandstone specimen, while the reduction extent has a significant relation to the fissure length and fissure angle.



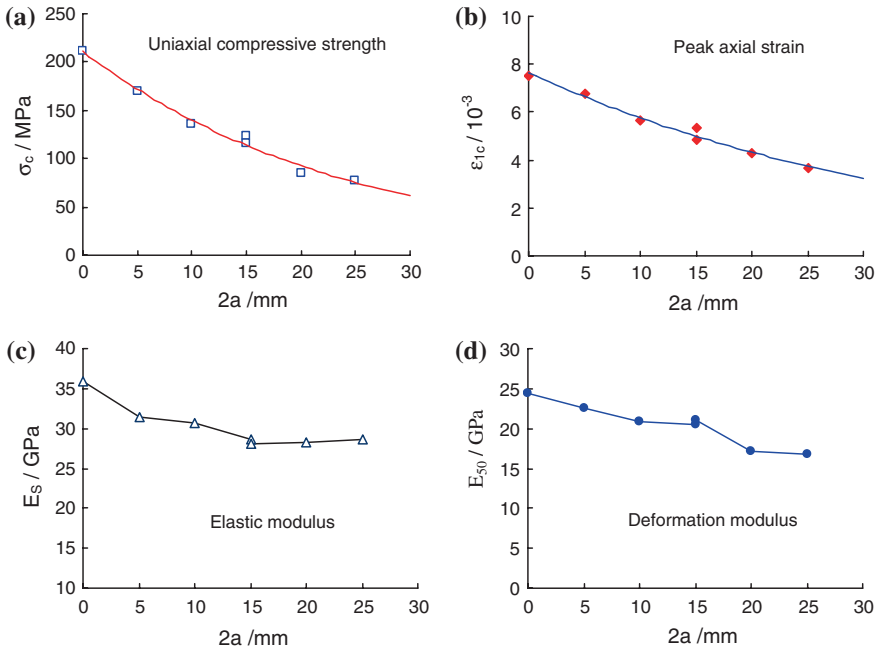


**Fig. 2.8** Effect of fissure length on the strength and deformation parameters of sandstone specimens with the same fissure angle ( $\alpha = 45^\circ$ ) under uniaxial compression (with kind permission of Springer Publisher)

The uniaxial compressive strength of intact specimen was 212.08 MPa, while it could be seen that the UCS of specimens containing single fissure ranged from 77.25 MPa ( $\alpha = 45^\circ$  and  $2a = 25$  mm) to 181.71 MPa ( $\alpha = 75^\circ$  and  $2a = 15$  mm), while the reduction extent of uniaxial compressive strength was between 14.3 and 63.6 %. In accordance with Fig. 2.8a, one can conclude that the uniaxial compressive strength will decrease with increase in fissure length. However, for the relation between uniaxial compressive strength and fissure angle, according to Fig. 2.9a, it can be seen that the uniaxial compressive strength first decreases and then increases with increasing fissure angle.

The intact sandstone specimen failed at a strain of 0.75 % under uniaxial compression, while sandstone specimens containing a single fissure failed at a strain of approximately 0.37–0.68 %, which is less than that of intact specimen. Moreover, the peak axial strain  $\epsilon_{1c}$  of sandstone specimen is dependent distinctly to fissure length and fissure angle. In accordance with Fig. 2.8b, one can conclude that the peak axial strain decreases with increase in fissure length. However, for the relation between peak axial strain and fissure angle, in accordance with Fig. 2.9b, it can be seen that  $\epsilon_{1c}$  has a nonlinear relation with the fissure angle.

The elastic modulus and deformation modulus of intact specimen were 35.95 and 24.37 GPa, respectively. However, the elastic modulus of specimen containing

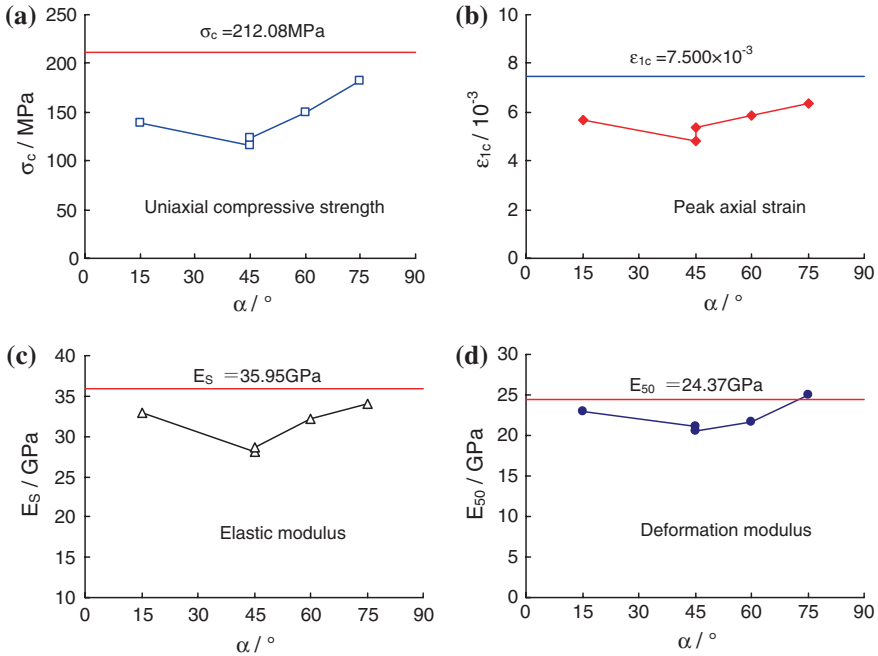


**Fig. 2.9** Effect of fissure angle on the strength and deformation parameters of sandstone specimens with the same fissure length ( $2a = 15$  mm) under uniaxial compression (with kind permission of Springer Publisher)

a single fissure ranged from 28.11 GPa ( $\alpha = 45^\circ$  and  $2a = 15$  mm) to 33.97 GPa ( $\alpha = 75^\circ$  and  $2a = 15$  mm), while the reduction extent of elastic modulus was between 5.5 and 21.8 %. The deformation modulus of specimen containing a single fissure ranged from 16.81 GPa ( $\alpha = 45^\circ$  and  $2a = 25$  mm) to 24.93 GPa ( $\alpha = 75^\circ$  and  $2a = 15$  mm), while the reduction extent of deformation modulus was between  $-2.3$  and 31 %. On the whole, the Young's modulus of sandstone has a decreasing trend with increase in fissure length, but a nonlinear relation with the fissure angle. Notice, for the fissured specimen with the same angle ( $\alpha = 45^\circ$ ), the elastic modulus of specimen tends to a stable value  $\sim 28$  GPa after the fissure length increases to 15 mm.

Among all the specimens containing single fissure, the deformation moduli of the specimens GS-14<sup>#</sup> ( $\alpha = 45^\circ$  and  $2a = 20$  mm) and GS-17<sup>#</sup> ( $\alpha = 45^\circ$  and  $2a = 25$  mm) are lowest and approximately 17 GPa, which results from the axial stress corresponding to an abrupt change of slope before peak strength is lower than half the peak strength. Except for the specimens GS-14<sup>#</sup> and GS-17<sup>#</sup>, the average deformation modulus of other specimens containing a single fissure is about 22.37 GPa, which reaches 91.8 % of the deformation modulus  $\sim 24.37$  GPa of intact specimen, and the dispersion coefficient (the percentage of the differential value between the maximum and minimum value to the average value) is approximately 18 %.

From the above analysis, one can conclude that, for the specimen with longer fissure or the fissure angle of  $45^\circ$ , the corresponding mechanical parameters are all lower, which shows that the longer fissure and fissure angle of  $45^\circ$  in the specimen have a significant effect on the strength and deformation parameters of sandstone specimen. Moreover, the influence of single fissure geometries on the uniaxial compressive strength and peak axial strain is higher than that on the Young's modulus for such brittle sandstone material.

## 2.3 Crack Evolution Behavior

In this chapter, the intact sandstone specimen leads to typically axial splitting failure (Fig. 2.6), which is a good agreement with many laboratory testing results of brittle rocks. It needs to be explained that we did not observe any crack coalescence for intact specimen before peak strength; moreover, the intact specimen failed in 2 s after peak stress and a huge failure sonic was heard during testing. At the same time, the intact specimen was fractured into many small blocks, see Fig. 2.6. However, for specimens containing a single fissure, under uniaxial compression, different failure modes were observed in comparison with that of intact specimen. The crack coalescence was all observed from upper and under tips of pre-existing fissure in sandstone specimens containing single fissure, and ultimate failure mode is distinctly dependent on the fissure length and fissure angle. Therefore, in this section, systematic evaluation is made on crack coalescence in sandstone specimens by photographic monitoring and AE technique.

### 2.3.1 Crack Coalescence Type of Sandstone Specimens Containing a Single Fissure

Nine different crack types (Fig. 2.10) were identified based on their geometry and crack propagation mechanism (tensile, shear, lateral crack, far-field crack, and surface spalling) by analyzing the ultimate failure modes of sandstone specimens containing a single fissure (Figs. 2.11 and 2.12). In accordance with Fig. 2.10, one can see that five of them (crack types I–VI) are tensile, one of them (crack type VI) is lateral crack, one of them (crack type VII) is shear, one of them (crack type VIII) is far-field, and one of them (crack type IX) is surface spalling. All crack types can be categorized as follows:

- (1) *Crack type I*: Wing crack initiates simultaneously from upper and under tips of single fissure. The tensile wing crack usually initiates along the vertical direction to pre-existing fissure, and then gradually departs toward the direction of axial stress, and finally develops along the direction of axial stress. Moreover, due to very fine grain sizes in sandstone material, this coalescence path of tensile wing crack I is very smooth.

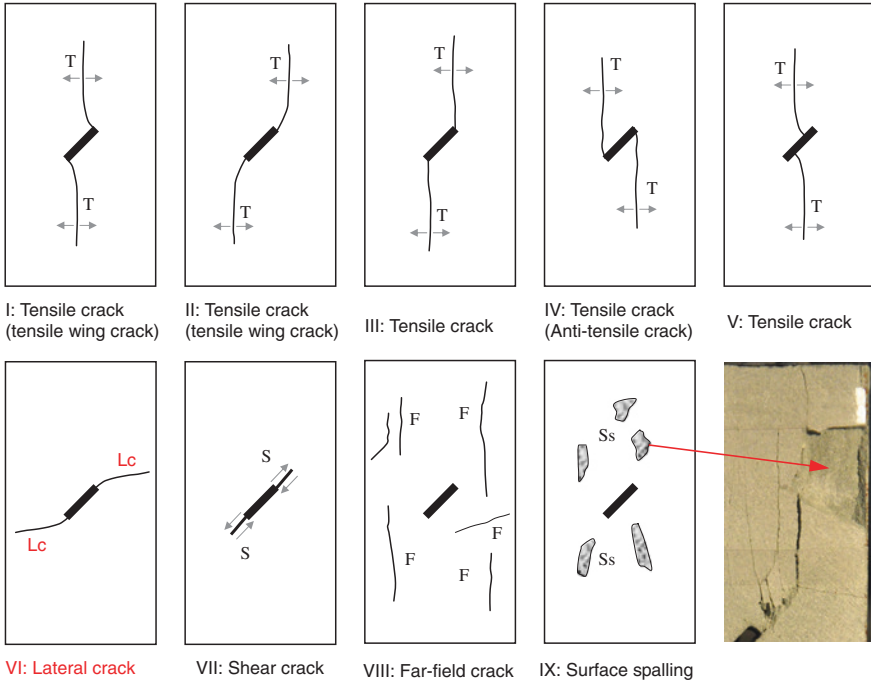


**Fig. 2.10** Various crack types from single fissure identified in this chapter. *T* Tensile crack, *Lc* Lateral crack, *S* Shear crack, *F* Far-field crack, *Ss* Surface spalling (with kind permission of Springer Publisher)

- (2) *Crack type II*: Wing crack often initiates simultaneously from upper and under tips of single fissure. The wing cracks initiate first along the direction of the fissure, and then gradually turn toward the direction of axial stress, and finally develop toward the end face of specimen.
- (3) *Crack type III*: Tensile crack initiates from upper or under tip of single fissure. Usually, the tensile crack III develops along the direction completely parallel to the axial stress, but the crack coalescence path is not very smooth.
- (4) *Crack type IV*: The crack coalescence is reverse to that of crack type III, which is referred to as “anti-tensile crack.” The anti-tensile crack also initiates from upper or under tip of single fissure, and develops along the direction of the axial stress.
- (5) *Crack type V*: The tensile crack usually initiates from this position which is located at a distance away from the tips of single fissure. The tensile crack initiates along the vertical direction to the fissure, and then gradually departs toward the direction of axial stress, and finally develops along the direction of axial stress.
- (6) *Crack type VI*: The crack initiates from upper or under tip of single fissure. The lateral crack initiates first along the direction to the fissure, and then

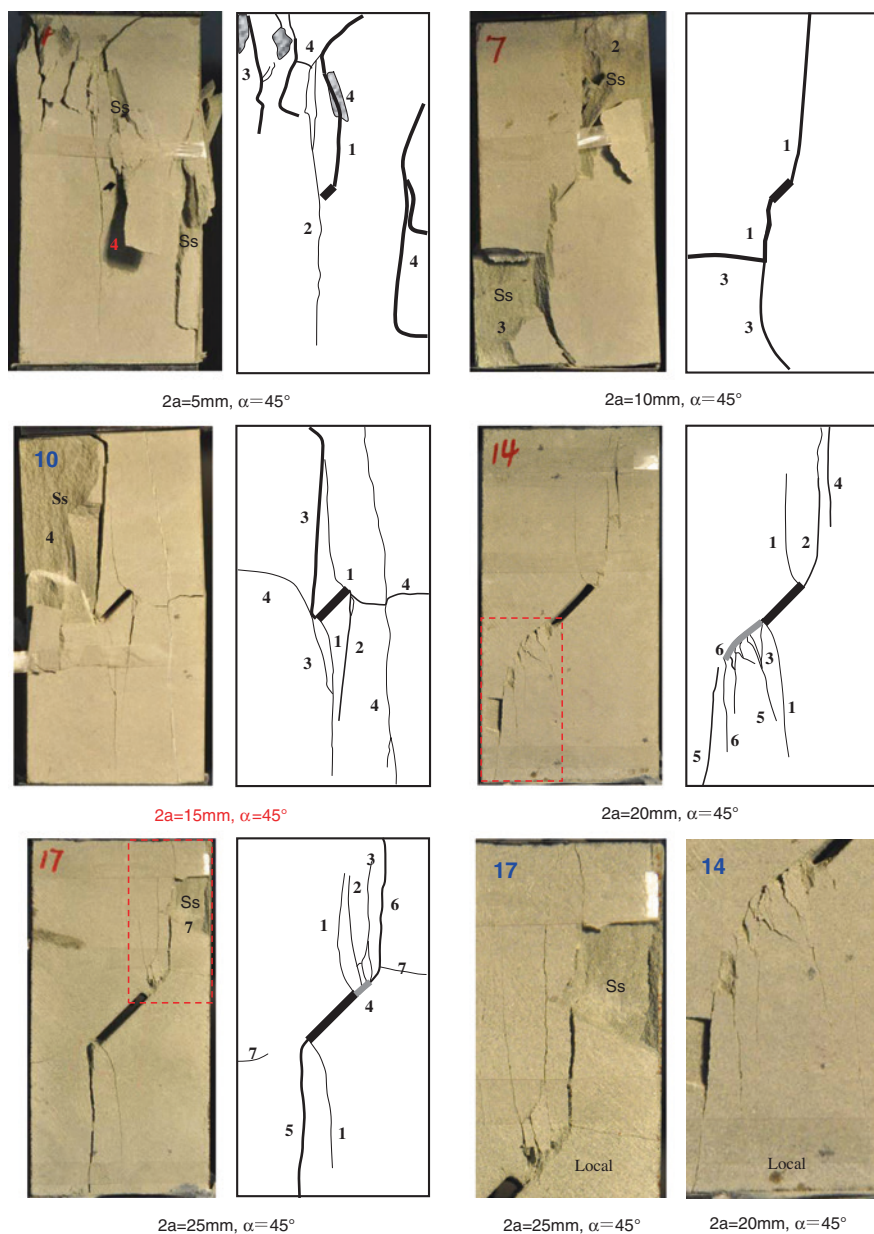


**Fig. 2.11** Effect of fissure length on ultimate failure modes of brittle sandstone specimens containing single fissure under uniaxial compression ( $\alpha = 45^\circ$ ) (with kind permission of Springer Publisher)

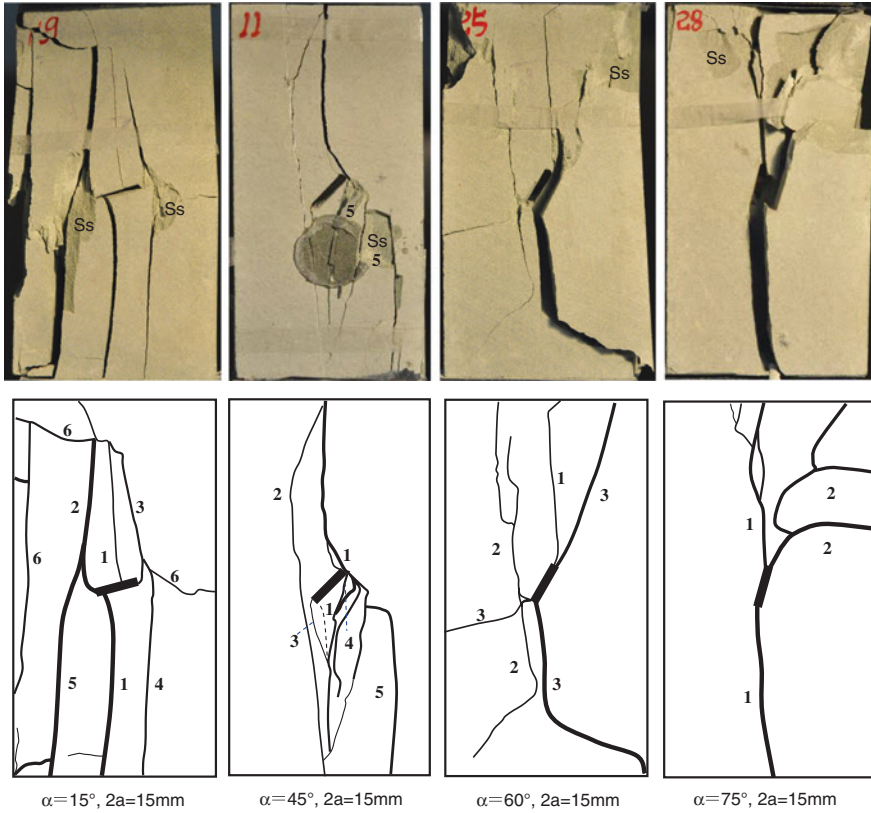


**Fig. 2.12** Effect of fissure angle on ultimate failure modes of brittle sandstone specimens containing single fissure under uniaxial compression ( $2a = 15 \text{ mm}$ ) (with kind permission of Springer Publisher)

gradually turns toward the horizontal direction, and finally develops toward the lateral face of specimen.

- (7) *Crack type VII*: The shear crack initiates from upper or under tip of single fissure, where the crack coalescence path is parallel to the direction of pre-existing fissure. The shear crack and pre-existing fissure are coplanar.
- (8) *Crack type VIII*: The far-field crack does not usually initiate from the tips of single fissure. Moreover, the far-field crack coalescence path is not very smooth, which may be vertical or horizontal in the process of loading.
- (9) *Crack type IX*: The surface spalling shown in Fig. 2.10 is often observed for brittle rock material. The surface spalling usually appears after some tensile cracks (such as crack types I–III) or accompanies with the process of tensile crack (such as crack type IV) propagation.

In accordance with the above nine crack types, one can analyze the ultimate failure mode and cracking process of sandstone specimens containing a single

**Table 2.3** Initiated crack types of sandstone specimens containing single fissure with different lengths and angles

Specimen	Crack types								
	I: Tensile	II: Tensile	III: Tensile	IV: Tensile	V: Tensile	VI: Lateral	VII: Shear	VIII: Far-field	IX: Surface spalling
GS-03 <sup>#</sup>	Intact specimen: typically axial splitting failure (Fig. 2.6)								
GS-04 <sup>#</sup>			√1					√	√ (more)
GS-07 <sup>#</sup>			√1					√	√ (more)
GS-10 <sup>#</sup>	√1		√	√		√		√	√ (more)
GS-14 <sup>#</sup>	√1	√	√				√	√	
GS-17 <sup>#</sup>	√1	√	√				√	√ (small)	√ (small)
GS-19 <sup>#</sup>			√	√	√1	√		√	√ (small)
GS-11 <sup>#</sup>	√1		√	√				√	√ (small)
GS-25 <sup>#</sup>			√1	√		√	√	√	√
GS-28 <sup>#</sup>			√1			√		√	√

Note √1 indicates that the crack is the first crack to initiate from the tips of pre-existing fissure

fissure under uniaxial compression (Figs. 2.11 and 2.12; Table 2.3). It is clear that the macroscopic failure mode of sandstone specimens containing a single fissure (Figs. 2.11 and 2.12) are all a mixture of several cracks among the above nine various crack types. For example, the failure mode of the specimen GS-17<sup>#</sup> ( $2a = 25$  mm,  $\alpha = 45^\circ$ ) is a mixture of cracks I–III and VII–IX. From Table 2.3, some qualitative conclusions can be summarized as follows.

Table 2.3 summarizes initiated crack types of sandstone specimens containing single fissure with different lengths and angles in response to the applied axial loads. As indicated in Table 2.3, tensile cracks I and III are often the first cracks to initiate from the tips of pre-existing fissure. But sometimes, the tensile crack V located at a distance away from the tips of single fissure is also the first crack, and is only observed in the specimen GS-19<sup>#</sup> ( $2a = 15$  mm,  $\alpha = 15^\circ$ ), which is possible to result from the heterogeneity of rock material or lower fissure angle. For tensile crack IV, it is clear that anti-tensile crack IV often accompanies with tensile crack III toward the reverse direction, which is usually observed in the specimen with fissure length of 15 mm.

It needs to be noted that tensile wing crack I is usually easier to initiate and nucleate from the tips of the longer fissures, e.g., the fissure length is 20 or 25 mm. Keeping the fissure length of the specimen 15 mm as a constant, only the specimen with fissure angle of  $45^\circ$  initiates tensile wing crack I from the tips of single fissure. Tensile wing crack II is observed only when the fissure length is equal to 20 or 25 mm. But surface spalling IX initiates in all other specimens containing single fissure except for the specimen GS-14<sup>#</sup>. However, the tensile crack III and far-field crack VIII are all observed in all the flawed specimens. The above phenomenon shows that cracks III, VIII–IX are easier to occur during loading for brittle rock material.



In accordance with Table 2.3, tensile crack V is rare, which is only observed in the specimen GS-19<sup>#</sup> ( $2a = 15$  mm,  $\alpha = 15^\circ$ ). Tensile crack IV initiates from the tips of fissure only when the fissure angle is lower than  $60^\circ$ , but lateral crack VI is only observed in specimens with fissure length of 15 mm except for the specimen GS-11<sup>#</sup>. Moreover, it can be concluded that shear crack VII usually occurs in specimens containing longer fissures, such as  $2a = 20$  or 25 mm. But sometimes, the shear crack VII is also observed in the fissured specimen ( $2a = 15$  mm,  $\alpha = 60^\circ$ ), which shows the fissure angle  $\sim 60^\circ$  makes the specimen easier to emanate the crack VII along the direction of pre-existing fissure.

From Figs. 2.11 and 2.12, it can also be seen that some wing cracks appear to be arrested a certain distance from the upper and lower boundaries of the specimen, which is probably related to the confining stress induced by friction between the specimen and the steel platen.

### 2.3.2 AE Behaviors of Intact and Flawed Sandstone Specimens with Single Fissure Geometries

AE monitoring is useful for exploring the failure process and crack coalescence mechanism of brittle rocks, especially for flawed rocks with pre-existing fissures. Therefore, during the uniaxial compression test, the AE technique is adopted for the sandstone specimens in this chapter.

Figure 2.13 shows the AE counts and AE energy of intact sandstone specimen during the whole deformation failure, however, Figs. 2.14, 2.15, 2.16, 2.17, and 2.18 show the AE counts of some typical sandstone specimens containing single fissure in the process of uniaxial compression test. In accordance with the AE results shown in Figs. 2.14, 2.15, 2.16, 2.17, and 2.18, a detailed investigation of the AE characteristics of brittle sandstone specimens with different fissure geometries was carried out. The AE characteristics of intact and flawed sandstone containing single fissure can be approximately divided into three typical periods, i.e., quiet period, active period, and remission period (Fig. 2.13a).

In the quiet period, the uniaxial compression stress–time curve of intact and fissured sandstone specimen all show the downward concave and the initial nonlinear deformation at low stress levels. Notice, the quiet period corresponds to the stage of fissure closure, therefore the AE events are not very active and the AE counts are also very rare compared with the active period, which results from only occurrence of fissure closure at this stage. Moreover, we can see that for hard and brittle sandstone material, the AE behavior at quiet period is not dependent on the fissure geometries, including fissure length and fissure angle.

In the active period, the stress–strain curves of sandstone specimens undergo two different stages, i.e., the stage of elastic deformation, and the stage of crack growth and propagation. With the increase of time, the axial stress increases linearly at the stage of elastic deformation, but when increasing to yielding stress, the axial stress–time curve occurs to depart from the linear curve and shows



**Fig. 2.13** AE counts and AE energy of intact sandstone specimen during the whole deformation failure. The number in *double bracket* in vertical axis labels is the multiplier of coordinates (with kind permission of Springer Publisher)

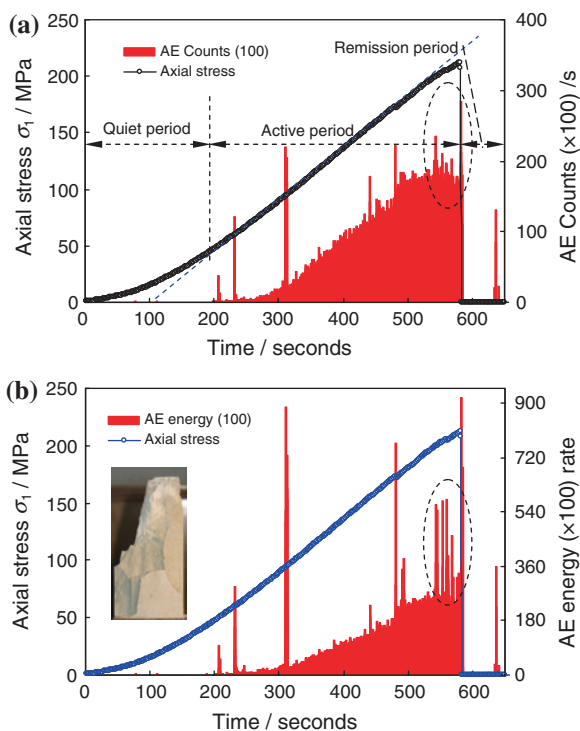
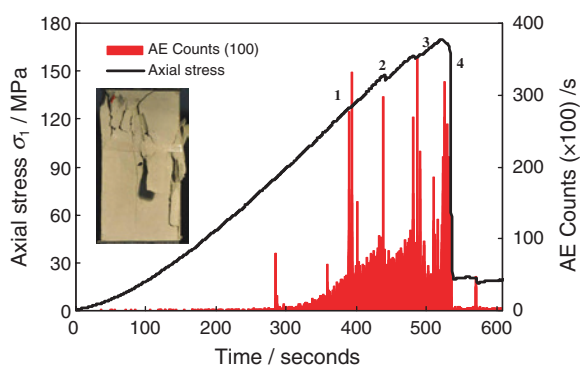


**Fig. 2.14** Relation between axial stress, AE counts, and time of sandstone specimen containing short fissure ( $2a = 5$  mm,  $\alpha = 45^\circ$ ) (with kind permission of Springer Publisher)



distinctly nonlinear behavior. For intact specimen (Fig. 2.13), the AE events are quite active, and the AE counts are dense and stable. Moreover, with the increase of axial stress, the AE counts and energy of intact specimen all increase continuously. But after yielding stress, although the AE counts of intact specimen do not increase with increase of time, the AE energy increases rapidly as shown in elliptical zone (Fig. 2.13), which further validates abrupt splitting failure of brittle sandstone (Fig. 2.6).

**Fig. 2.15** Relation between axial stress, AE counts, and time of sandstone specimen containing medium fissure ( $2a = 15\text{ mm}$ ,  $\alpha = 45^\circ$ ) (with kind permission of Springer Publisher)

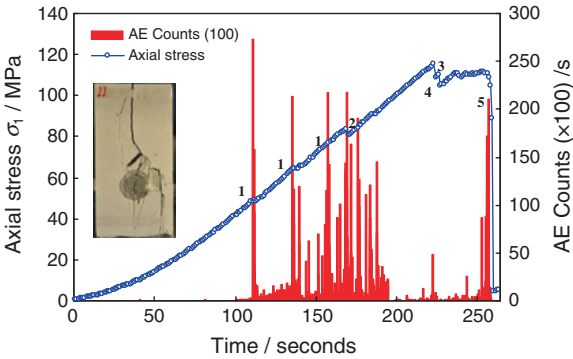
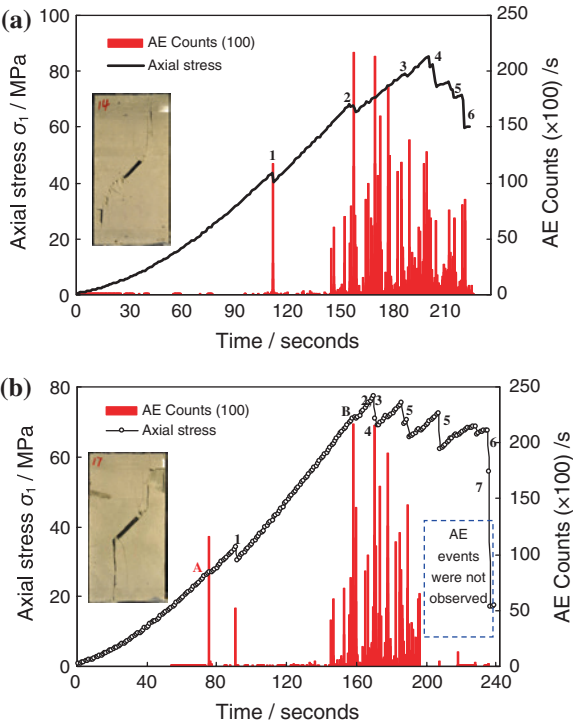


**Fig. 2.16** Relation between axial stress, AE counts, and time of sandstone specimen containing the longer fissure  
**a**  $2a = 20\text{ mm}$ ,  $\alpha = 45^\circ$ ;  
**b**  $2a = 25\text{ mm}$ ,  $\alpha = 45^\circ$ . *Note* the AE counts in the square were not observed (with kind permission of Springer Publisher)



However, for flawed specimen with single fissure (Figs. 2.14, 2.15, 2.16, 2.17 and 2.18), the AE behaviors during deformation failure are different from that of intact specimen (Fig. 2.13) in the active period, which is distinctly related to fissure length and fissure angle. The AE counts of flawed specimen with single fissure are more decentralized than that of intact specimen; moreover, the AE counts of all flawed specimens with single fissure have several larger peak values before peak strength, which correspond to the crack initiation and propagation in the specimens. Notice, the quiescence of the AE observed before the failure is probably due to the

**Fig. 2.17** Relation between axial stress, AE counts, and time of sandstone specimen containing lower angles ( $2a = 15 \text{ mm}$ ,  $\alpha = 15^\circ$ ) (with kind permission of Springer Publisher)

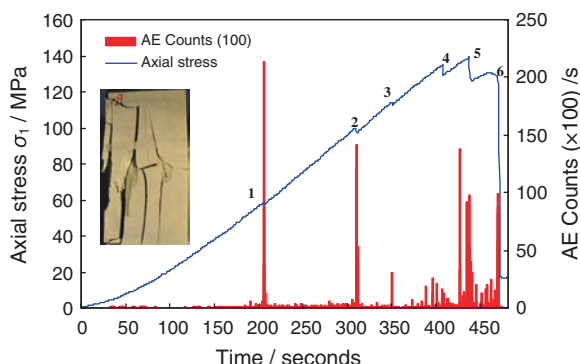
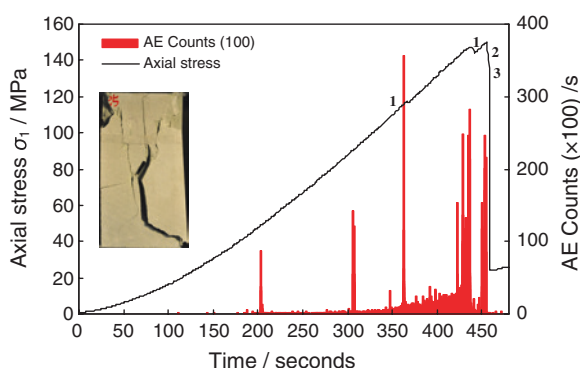


**Fig. 2.18** Relation between axial stress, AE counts and time of sandstone specimen containing higher angles ( $2a = 15 \text{ mm}$ ,  $\alpha = 60^\circ$ ) (with kind permission of Springer Publisher)



increasing attenuation as cracks propagate. This is often observed particularly when spalling occurs near the surface (Wassermann et al. 2009).

In accordance with the AE counts shown in Figs. 2.14, 2.15 and 2.16, one can conclude that the fissure length has great influence on the AE behavior in the active period. When the fissure length is shorter ( $2a = 5 \text{ mm}$ ) in Fig. 2.14, the dense extent of AE counts of flawed specimen is approximately similar to that of intact specimen (Fig. 2.13a), but the flawed specimen has several larger peak values. For the specimens containing medium fissure ( $2a = 15 \text{ mm}$ ) in Fig. 2.15, several larger peak values of AE signals are observed at the stage of elastic deformation, while AE counts are very rare at the stage of crack growth and propagation, which shows that there is no distinct crack coalescence at this stage. However, for specimens containing longer fissures ( $2a = 20, 25 \text{ mm}$ ) as shown in Fig. 2.16, the AE behavior is reverse to that of flawed specimens ( $2a = 15 \text{ mm}$ ), whereby the AE events are not active and AE counts are very rare at the stage of elastic deformation, but very dense at the stage of crack growth and propagation.

From Figs. 2.17 to 2.18, one can also see the effect of fissure angle on the AE behaviors at the active period. For flawed specimens with lower angle ( $\alpha = 15^\circ$ ), the AE events are not very active and AE counts are very rare except for

several larger AE peak values. However, for flawed specimens with larger angle ( $\alpha = 60^\circ$ ), the AE behaviors are approximately the same as that with lower angle ( $\alpha = 15^\circ$ ) at the stage of elastic deformation, while the AE counts at the stage of crack growth and propagation are more and denser than that with lower angle ( $\alpha = 15^\circ$ ).

At the remission period (i.e., the stage of strain-softening), the AE counts and energy of intact specimen are rare. The AE behaviors of flawed specimen with shorter fissure ( $2a = 5$  mm) or higher angle ( $\alpha = 60^\circ$ ) are approximately the same as that of intact specimen, which results from little occurrence of macroscopic cracks after peak strength. But, the AE behaviors of flawed specimen with medium fissure ( $2a = 15$  mm) are not dependent on the fissure angle, which shows that the AE counts undergo first a relative steady phase and then increase abruptly with increasing time, as shown in Figs. 2.15 and 2.17. However, for flawed specimen with longer fissure ( $2a = 20$  and  $25$  mm), it can be seen from Fig. 2.16 that the AE counts are more and relatively denser, which results from gradual crack coalescence in the specimens after peak strength. It needs to be noted that the AE events in the square in Fig. 2.16b were not observed, which is due to the departure between AE sensor and specimen surface.

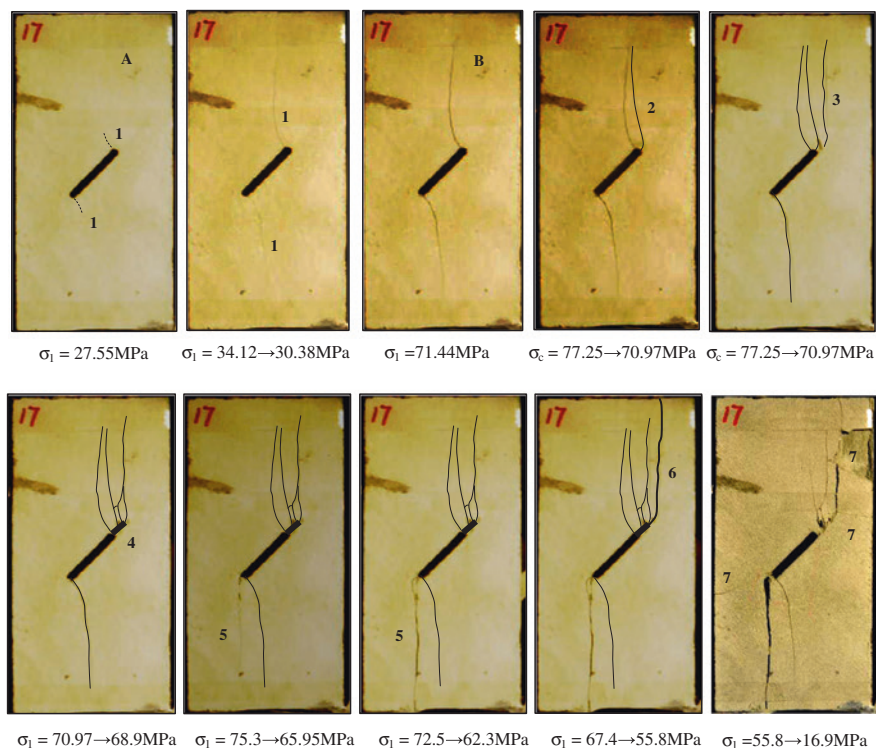
In sum, the above analysis shows clearly that the AE behaviors of specimen are closely dependent on the crack coalescence in the specimen, which will be analyzed and discussed detailed in the following section.

### 2.3.3 Real-Time Crack Evolution Process of Sandstone Containing a Single Fissure

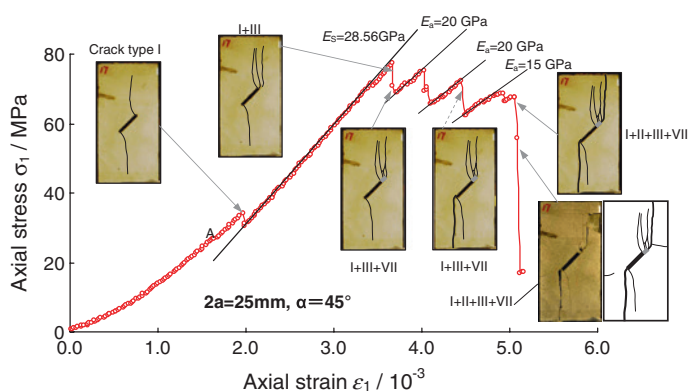
Besides the previous AE technique, photographic monitoring was also adopted during uniaxial compression test to clarify further the precedence relationship of crack coalescence in sandstone specimen. Based on the combined results on AE and photographic monitoring, the real-time crack coalescence process of sandstone containing a single fissure can result in a more detailed analysis as follows.

Figure 2.19 shows typical real-time crack coalescence process of sandstone specimens containing a single fissure ( $2a = 25$  mm,  $\alpha = 45^\circ$ ) using photographic monitoring. From Fig. 2.19, it is clear that photographic monitoring can be used to identify and characterize the crack coalescence process of flawed sandstone. Notice the denoted number and letter shown in Fig. 2.19 are corresponding to Fig. 2.16b. Figure 2.20 shows the influence of real-time crack coalescence on the strength and deformation failure behavior of sandstone specimens containing a single fissure ( $2a = 25$  mm,  $\alpha = 45^\circ$ ) under uniaxial compression.

In accordance with Fig. 2.16b and Figs. 2.19, 2.20, we can analyze real-time crack coalescence process of sandstone specimen containing a single fissure ( $2a = 25$  mm,  $\alpha = 45^\circ$ ). Before point A ( $\sigma_1 = 27.55$  MPa =  $35.7\% \sigma_c$ ) as shown in Fig. 2.16, the stress concentration at the tips of fissure does not reach the material strength nearby the tips, which does not result in a crack initiation. But when



**Fig. 2.19** Typical real-time crack coalescence process of sandstone specimen containing a single fissure ( $2a = 25 \text{ mm}$ ,  $\alpha = 45^\circ$ ). The denoted number and letter shown in the figure are corresponding to Fig. 2.16b (with kind permission of Springer Publisher)



**Fig. 2.20** Effect of real-time crack coalescence on the strength and deformation behavior of sandstone specimens containing a single fissure ( $2a = 25 \text{ mm}$ ,  $\alpha = 45^\circ$ ) under uniaxial compression (with kind permission of Springer Publisher)

the axial stress is loaded to point A, the specimen begins to initiate the wing crack I from the upper and under tips of fissure, but the crack is too fine to be observed with the unaided eyes or in video recordings. Notice the initiated stress of wing crack I is identified by AE counts, as shown in Fig. 2.16b. After point A, with the increase in axial deformation, the wing crack I further lengthens and propagates gradually to the edge of the specimen. When the specimen is loaded to 34.12 MPa ( $44.2\% \sigma_c$ ), the wing crack I undergoes a large and rapid evolution to the edge of the specimen, which leads to the axial supporting capacity dropping to 30.38 MPa in a smaller range of axial strain. Afterwards, with the increase of axial deformation, the wing crack I is difficult to lengthen due to the limitation of specimen boundary, but widens a lot. The continuous increase in deformation leads to the specimen being loaded to 77.25 MPa ( $100\% \sigma_c$ ). At this moment of about 171 s, cracks 2–3 (crack type III) develop rapidly to the edge of specimen in one second, and two subsequent tensile cracks III can only be snapped with photographic monitoring.

However, after the specimen is loaded to peak strength, the axial supporting capacity does not drop to zero. For the moment, the axial stress of this specimen is about 70.97 MPa and corresponding axial strain is  $\sim 3.67 \times 10^{-3}$ . Notice, the specimen still has a supporting structure (Fig. 2.20). Afterwards, with the increase of axial deformation, shear crack VII emanates from the upper tip of fissure and the corresponding axial stress drops rapidly from 70.97 to 68.9 MPa. At this time, the axial supporting capacity begins to increase slowly with increasing deformation. While due to obvious damage of supporting structure, the reloading average modulus  $\sim E_a$  (about 20 GPa) is distinctly lower than the elastic modulus ( $\sim 28.56$  GPa) before peak strength. When the specimen reaches the axial stress  $\sim 75.3$  MPa, crack 5 (crack type III) begins to initiate and propagate from the under tip of fissure along the direction of axial loading, which leads to the axial supporting capacity dropping to 65.95 MPa in a small range of axial strain. Afterwards, with increasing axial deformation, the axial stress begins to increase slowly and the reloading average modulus is approximately equal to 20 GPa, which indicates that the initiation and coalescence of crack 5 does not affect the average modulus, but reduces the axial supporting capacity of fractured rock. With the increase of axial deformation, the axial supporting capacity begins to increase slowly. But due to more obvious damage of supporting structure, the reloading average modulus (15 GPa) is distinctly lower than the previous average modulus (20 GPa) and the axial stress–axial strain begins to depart gradually toward the axial strain. When the specimen was loaded to 67.4 MPa (corresponding axial strain is  $5.06 \times 10^{-3}$ ), crack 6 (crack type II) occurs very fast. The axial stress of the specimen drops to 55.8 MPa and corresponding axial strain is  $5.09 \times 10^{-3}$ . Finally, with the increase of axial deformation, some far-field crack VIII and surface spalling IX are also observed, which results in rapid reduction of axial supporting capacity until 16.9 MPa in an almost constant axial strain.

Using photographic monitoring, Fig. 2.21 also presents the influence of real-time crack coalescence on the strength and deformation failure behavior of sandstone specimens containing a single fissure ( $2a = 15$  mm,  $\alpha = 15^\circ$ ) under uniaxial compression. Notice the denoted number shown in Fig. 2.21 is corresponding to Fig. 2.17.

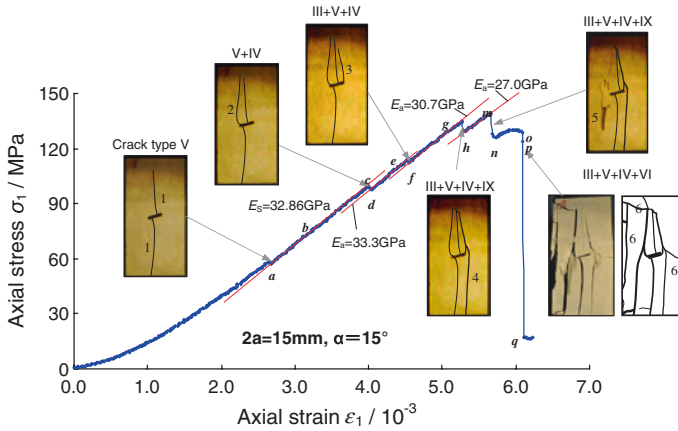


**Fig. 2.21** Effect of real-time crack coalescence on the strength and deformation behavior of sandstone specimens containing a single fissure ( $2a = 15$  mm,  $\alpha = 15^\circ$ ) under uniaxial compression (with kind permission of Springer Publisher)

Comparing Fig. 2.21 with Fig. 2.20, it can be seen that more main crack coalescences shown in Fig. 2.20 occur after peak strength, while more main crack coalescences in Fig. 2.21 take place before peak strength, which results from the difference of fissure length and angle in the specimen.

In accordance with Fig. 2.21, we can also analyze real-time crack coalescence process of sandstone specimen containing a single fissure ( $2a = 15$  mm,  $\alpha = 15^\circ$ ). Before point *a* ( $\sigma_1 = 58.40$  MPa = 41.9 % $\sigma_c$ ) as shown in Fig. 2.21, the stress concentration at the tips of fissure does not reach the material strength nearby the tips, which does not result in crack initiation. But when the axial stress is loaded to point *a*, the specimen begins to produce rapidly wing crack 1 (crack type V) from the upper and under tips of fissure, which can be observed with the naked eyes. When crack 1 propagates to the edge of the specimen, the axial stress undergoes a minor drop to 57.4 MPa from 58.4 MPa. After point *a*, crack 1 is difficult to lengthen due to the limitation of specimen boundary. The axial stress increases linearly with axial deformation as the elastic modulus of 32.86 GPa (Fig. 2.22a). When the specimen is loaded to point *c* ( $\sigma_1 = 99.9$  MPa = 71.7 % $\sigma_c$ ), crack 2 (crack type IV) produces from the under tip of fissure and propagates toward the upper edge of the specimen rapidly, which leads to the corresponding axial stress dropping rapidly from 99.9 to 98.4 MPa. At this time, the specimen has still a good supporting structure. Therefore, with increase of axial deformation, the axial supporting capacity begins to increase with approximately the same average modulus ~33.3 GPa (Fig. 2.22b) as elastic modulus ~32.86 GPa (Fig. 2.22a), which indicates that the initiation and propagation of cracks 1–2 have no influence on the elastic deformation behavior of the specimen. When the specimen is loaded to point *e* ( $\sigma_1 = 114.2$  MPa = 82 % $\sigma_c$ ), crack 3 (crack type III) emanates from the upper tip of fissure and the corresponding axial stress drops rapidly from 114.2



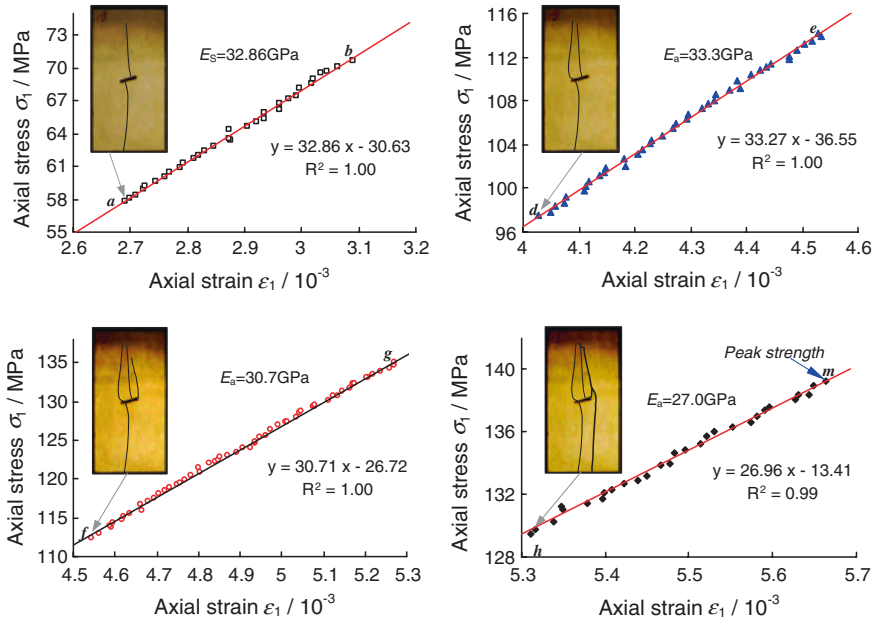


**Fig. 2.22** Relation between axial stress and axial strain after several crack coalescences in brittle sandstone specimen containing a single fissure ( $2a = 15$  mm,  $\alpha = 15^\circ$ ) under uniaxial compression (All the *symbols* represent experimental results and the *lines* represent the regression results) (with kind permission of Springer Publisher)

to 112.4 MPa. Afterwards, the axial supporting capacity begins to increase slowly with increasing deformation; while due to some minor damage of supporting structure, the reloading average modulus  $\sim 30.7$  GPa (Fig. 2.22c) is a little lower than the elastic modulus ( $\sim 32.86$  GPa).

Afterwards, when the specimen is loaded to point *g* ( $\sigma_1 = 135.1$  MPa = 97 % $\sigma_c$ ), crack 4 (crack type IV) emanates from the upper tip of fissure and the corresponding axial stress drops rapidly from 135.1 to 129.4 MPa. For the moment, the axial supporting capacity begins to increase slowly with increasing deformation; while due to obvious damage of supporting structure, the reloading average modulus  $\sim 27.0$  GPa (Fig. 2.22d) is distinctly lower than the elastic modulus ( $\sim 32.86$  GPa). The continuous increase of deformation leads to the specimen being loaded to 139.28 MPa (100 % $\sigma_c$ ), at this moment, crack 5 (crack type III) develops rapidly in 1 s, which leads to the axial supporting capacity dropping to 127.7 MPa in a smaller range of axial strain. From Fig. 2.22, we can see clearly that the axial stress of the specimen has a better linear relation with the axial strain after each larger crack coalescence in the specimen, which results probably from a kind of brittle and hard sandstone material in this chapter. However, after peak strength, the relation between axial stress and axial strain shown in Fig. 2.23 is distinctly different from that shown in Fig. 2.22. After axial stress of the specimen drops to point *n* ( $\sigma_1 = 126.22$  MPa = 90.6 % $\sigma_c$ ) from



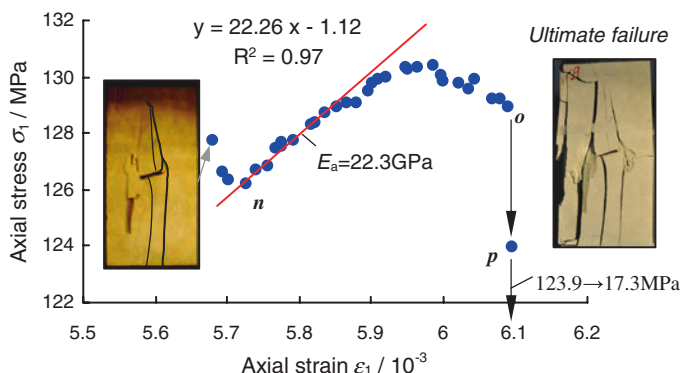


**Fig. 2.23** Relation between axial stress and axial strain in brittle sandstone specimen containing a single fissure ( $2a = 15$  mm,  $\alpha = 15^\circ$ ) after peak strength under uniaxial compression (with kind permission of Springer Publisher)

127.7 MPa, the axial supporting capacity begins to increase slowly with increase of axial deformation. But due to more obvious damage of supporting structure, the reloading average modulus (22.26 GPa) is distinctly lower than the previous average modulus (27 GPa) and the axial stress–axial strain begins to depart gradually toward the axial strain. When the specimen was loaded to point *o*, crack 6 occurs very fast. The axial stress of the specimen drops to 17.3 MPa and the corresponding axial strain is  $6.10 \times 10^{-3}$ . Moreover, some far-field crack VIII and surface spalling IX are also observed, which results in rapid reduction of axial supporting capacity until 17.3 MPa in an almost constant axial strain.

By adopting the same method as specimen GS-17# ( $2a = 25$  mm,  $\alpha = 45^\circ$ ) and GS-19# ( $2a = 15$  mm,  $\alpha = 15^\circ$ ), the real-time crack coalescence process of all other specimens with a single fissure can also be identified and characterized on the basis of photographic monitoring and AE technique. Table 2.4 summarizes the successive axial stress values of crack coalescence in the sandstone specimens containing a single fissure. In Table 2.4, numbers 1–7 represent the succession of crack coalescence, which corresponds to that shown in Figs. 2.11 and 2.12. It can be seen that each larger stress drop in the axial stress–axial strain curve indicates a larger crack propagation, which also corresponds to a larger amplifying of AE counts. Notice the initiation, propagation, and coalescence of some cracks occur after peak strength, which shows the re-fracture mechanical behavior of flawed specimen after failing. Moreover, the corresponding axial stress of initiating the first crack is closely dependent on fissure length and fissure angle. With increase of fissure length, the corresponding axial stress of initiating the first crack tends to decrease except for the specimen GS-10#, which shows that the initiation of the first crack in the specimen with longer fissure is easier than with shorter fissure. However, the corresponding axial stress of initiating the first crack has a nonlinear relation with the fissure angle, but for specimen GS-11# with  $\alpha = 45^\circ$ , the corresponding axial stress is lowest in all the specimens with fissure length of 15 mm

**Table 2.4** Succession of crack coalescence in sandstone specimen containing single fissure

Specimen	Subsequence/corresponding axial stress formed the crack in the specimen (Unit: MPa)						
	1	2	3	4	5	6	7
GS-04#	III (128.2)	VIII (148 → 144.3)	VIII, IX (170.04 = $\sigma_c$ )	VIII, IX (160.9 → 68.3)			
GS-07#	III (95.93 → 88.45)	IX (103.9, 136.39 = $\sigma_c$ , 135.2 → 133)	VIII, IX (112.17 → 8.49)				
GS-10#	I (101.6')	IV (120.8 → 118)	III, IV (122.8 = $\sigma_c$ → 90.8)	VI, VIII, IX (89.8 → 12.9)			
GS-14#	I (43.77 <sup>i</sup> → 40.35)	II (67.73 → 65.5)	III (79.28 → 78.4)	VIII (85.29 = $\sigma_c$ → 81.7)	VIII, III (76.1 → 73.6)	VII, III (69.5 → 59.8)	
GS-17#	I (27.55 <sup>i</sup> , 34.12 → 30.38)	III (77.25 = $\sigma_c$ → 70.97)	III (77.25 = $\sigma_c$ → 70.97)	VII (70.97 → 68.9)	III (75.3 → 65.95, 72.5 → 62.3)	II (67.4 → 55.8)	VIII, IX (55.8 → 16.9)
GS-19#	V (58.4 <sup>i</sup> → 57.4)	IV (99.9 → 98.4)	III (114.2 → 112.4)	IV, IX (135.1 → 129.4)	III, IX (139.28 = $\sigma_c$ → 127.7)	VI, VIII, IX (123.9 → 17.3)	
GS-11#	I (49.2 <sup>i</sup> , 64.3)	VIII (83.9 → 80.7)	III (115.17 = $\sigma_c$ → 108.9)	IV, IX (109.9 → 104.6)	VIII, IX (88.8 → 4.4)		
GS-25#	III (117 <sup>i</sup> , 146.57 → 144.3)	III, IV (149.96 = $\sigma_c$ → 143.6)	III, VI-IX (143.6 → 122.1 → 24)				
GS-28#	III (103.54 <sup>i</sup> → 101.1, 181.71 = $\sigma_c$ → 179.9)	VI, VII, IX (179.9 → 22.8)					

Note The letter *i* indicates the initiated axial stress of the first crack

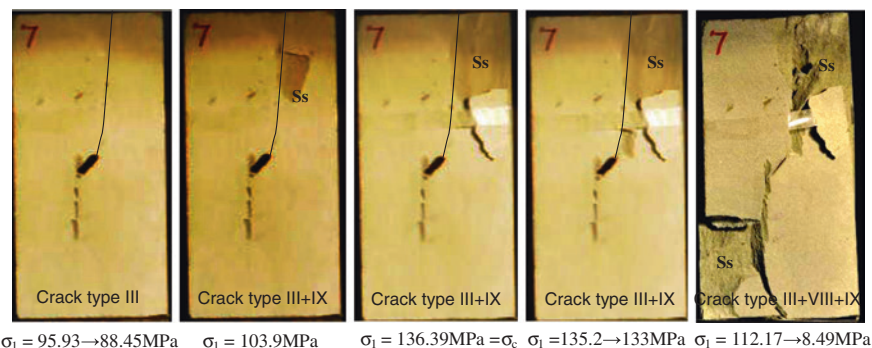


**Fig. 2.24** Typical real-time crack coalescence process of sandstone specimen containing a single fissure ( $2a = 10$  mm,  $\alpha = 45^\circ$ ) (with kind permission of Springer Publisher)

to initiate the first crack. Moreover, the heterogeneity of sandstone material has a significant effect on the axial stress to initiating the first crack.

In accordance with Table 2.4, one can further conclude that more crack coalescences occur in the specimens with longer fissure or smaller fissure angle, which indicates that the localization deformation failure (Fig. 2.5) is easier to initiate in specimens with longer fissure or smaller fissure angle. For the specimen with shorter fissure (e.g. GS-07<sup>#</sup>) as shown in Fig. 2.24, the surface spalling IX often occurs in brittle rock material but does not complete at once. From Fig. 2.24, it can be seen that surface spalling IX in the specimen GS-07<sup>#</sup> undergoes four processes with increase of axial deformation.

## 2.4 Conclusions

The aim of this chapter is to investigate the strength, deformation failure, and crack coalescence behavior in brittle sandstone material containing a single fissure under uniaxial compression by photographic monitoring and AE technique. On the basis of the experimental results of sandstone specimens containing a single fissure, the following conclusions can be drawn.

The fissure length and fissure angle have a key effect on the strength and deformation behavior of sandstone specimens under uniaxial compression. In this chapter, tested intact sandstone specimen is a kind of typical brittle rock and takes on typically axial splitting failure. Compared with intact specimen, the flawed specimen containing a single fissure fails with lower strengths, smaller Young's modulus, and smaller peak axial strain, which is closely related to the fissure length and fissure angle. Moreover, the flawed specimen takes on the localization deformation failure behavior. The mechanical parameters of flawed sandstone decrease with increase in fissure length, but first decrease and then increase with

increasing fissure angle. Moreover, the influence of single fissure geometries on the uniaxial compressive strength and peak axial strain is higher than that on the Young's modulus for such brittle sandstone material.

Nine different crack types are identified based on their geometry and crack propagation mechanism (tensile, shear, lateral crack, far-field crack, and surface spalling) for single fissure in response to the applied axial loads. Tensile cracks I and III are often the first cracks to initiate from the tips of pre-existing fissure. But sometimes, tensile crack V is also the first crack, and is only observed in the specimen GS-19<sup>#</sup> ( $2a = 15$  mm,  $\alpha = 15^\circ$ ), which shows that this fissure angle makes the specimen easier to emanate this tensile crack V. Tensile crack IV initiates from the tips of fissure only when the fissure angle is lower than  $60^\circ$ , but lateral crack VI is only observed in the specimens with fissure length of 15 mm except for one specimen GS-11<sup>#</sup>. However, anti-tensile crack IV often accompanies tensile crack III toward the reverse direction. The shear crack VII usually occurs in specimens containing longer fissures, while cracks III, VIII–IX are easier to occur during loading for brittle rock material. In accordance with nine crack types, the failure mode of flawed sandstone specimen containing single fissure under uniaxial compression is analyzed. The failure modes of flawed specimens are all a mixture of several cracks among nine crack types.

According to AE monitoring results in the process of deformation failure, the AE characteristics of intact and flawed sandstone containing single fissure can be approximately divided into three typical periods, i.e., quiet period, active period, and remission period. In quiet period, for hard and brittle sandstone material, the AE events are not very active and the AE counts are very small, which results from the occurrence of fissure closure. Moreover, the AE behavior in quiet period is not dependent on the fissure length and fissure angle. In the active period, the AE counts of intact specimen are very dense and stable, but the AE behaviors of flawed specimens are different from that of intact specimen, which is distinctly related to fissure length and fissure angle. The AE counts of flawed specimen with single fissure are more decentralized than that of intact specimen; moreover, the AE counts of all flawed specimens with single fissure have several larger peak values before peak strength, which correspond to the crack initiation and propagation in the specimens. However, in the remission period, the AE counts and energy of intact specimen are rare, but AE behaviors of flawed specimen with shorter fissure ( $2a = 5$  mm) or higher angle ( $\alpha = 60^\circ$ ) approximate the one of intact specimen, which results from little occurrence of macroscopic cracks after peak strength. While the AE behaviors of flawed specimen with medium fissure ( $2a = 15$  mm) are not dependent on the fissure angle, which shows that the AE counts undergo first a relative steady phase and then increase abruptly with increasing time. For flawed specimen with longer fissure ( $2a = 20$  and  $25$  mm), the AE counts are more and relatively denser, which results from gradual crack coalescence in the specimens after peak strength.

In order to confirm the subsequence of crack coalescence in sandstone specimen, photographic monitoring was adopted during uniaxial compression test. On the basis of the photographic monitoring results, the real-time crack coalescence

process of sandstone containing a single fissure is identified and characterized. Moreover, the corresponding axial stress of crack coalescence in the sandstone specimens containing a single fissure is also obtained. Each larger stress drop in the axial stress–axial strain curve indicates a larger crack propagation, which also corresponds to a larger amount of AE counts. The corresponding axial stress of initiating the first crack is closely dependent on fissure length and fissure angle. With the increase in fissure length, the corresponding axial stress of initiating the first crack tends to decrease except for specimen GS-10<sup>#</sup>, which shows that the initiation of the first crack in the specimen with longer fissure is easier than that with shorter fissure. However, the corresponding axial stress of initiating the first crack has a nonlinear relation with the fissure angle, but for specimen GS-11<sup>#</sup> with  $\alpha = 45^\circ$ , the corresponding axial stress is the lowest in all specimens of fissure length 15 mm to initiate the first crack. Lastly, two typical effects of real-time crack coalescence on the strength and deformation failure behavior of brittle sandstone specimen are analyzed under uniaxial compression.

This chapter investigates only the strength failure and crack coalescence behavior of brittle sandstone containing a single fissure of different lengths and angles under uniaxial compression by photographic monitoring and AE technique. In order to understand in-depth the failure behavior and fracture mechanism of engineering rock mass, more experimental investigations for flawed brittle sandstone specimens with two or three fissures (varying ligament angle, ligament length, fissure angle, fissure length, etc.) will be presented by advanced techniques (such as AE technique, photographic monitoring, etc.) in the following chapters.

## References

- Fairhurst CE, Hudson JA (1999) Draft ISRM suggested method for the complete stress–strain curve for the intact rock in uniaxial compression. *Int J Rock Mech Min Sci* 36(3):279–289
- Li YP, Chen LZ, Wang YH (2005) Experimental research on pre-cracked marble under compression. *Int J Solids Struct* 42:2505–2516
- Wassermann J, Senfaute G, Amitrano D et al (2009) Evidence of dilatant and non-dilatant damage processes in oolitic iron ore: P-wave velocity and acoustic emission analyses. *Geophys J Int* 177(3):1343–1356
- Yang SQ, Jiang YZ (2010) Triaxial mechanical creep behavior of sandstone. *Min Sci Technol* 20(3):339–349
- Yang SQ, Jing HW (2011) Strength failure and crack coalescence behavior of brittle sandstone samples containing a single fissure under uniaxial compression. *Int J Fract* 168(2):227–250

Strength Failure and Crack Evolution Behavior of Rock  
Materials Containing Pre-existing Fissures

Yang, S.-Q.

2015, XIV, 246 p. 182 illus., 168 illus. in color.,

Hardcover

ISBN: 978-3-662-47302-3